

## On Hydrodynamic Motions in Dead Zones

Jeffrey S. Oishi

*Department of Astronomy, 601 Campbell Hall, University of California at Berkeley,  
Berkeley, CA, 94720-3411*

`jsoishi@astro.berkeley.edu`

and

Mordecai-Mark Mac Low

*Department of Astrophysics, American Museum of Natural History, 79th Street at Central  
Park West, New York, NY 10024-5192*

`mordecai@amnh.org`

### ABSTRACT

We investigate fluid motions near the midplane of vertically stratified accretion disks with highly resistive midplanes. In such disks, the magnetorotational instability drives turbulence in thin layers surrounding a resistive, stable dead zone. The turbulent layers in turn drive motions in the dead zone. We examine the properties of these motions using three-dimensional, stratified, local, shearing-box, non-ideal, magnetohydrodynamical simulations. Although the turbulence in the active zones provides a source of vorticity to the midplane, no evidence for coherent vortices is found in our simulations. It appears that this is because of strong vertical oscillations in the dead zone. By analyzing time series of azimuthally-averaged flow quantities, we identify an axisymmetric wave mode particular to models with dead zones. This mode is reduced in amplitude, but not suppressed entirely, by changing the equation of state from isothermal to ideal. These waves are too low-frequency to affect sedimentation of dust to the midplane, but may have significance for the gravitational stability of the resulting midplane dust layers.

*Subject headings:* protoplanetary disk, magnetohydrodynamics

## 1. Introduction

A long standing problem in star formation concerns the accretion of high-angular momentum material in disks around protostars. The rediscovery of the magnetorotational instability (MRI) in an astrophysical context, along with the discovery of the favorable transport properties of the turbulence that results from it (Hawley et al. 1995) led to the widespread belief that a solution to this puzzle had been found. However, the instability requires a critical coupling strength between field and fluid (Blaes & Balbus 1994; Jin 1996). Noting the high densities and low temperatures likely at the midplanes of protoplanetary disks, Gammie (1996) developed a model including a weakly-coupled, MRI-stable “dead zone” at the midplane of such disks. Since this prediction, considerable effort has gone into elucidating the conditions under which such a model might exist. Most of this work has centered on chemical studies of the conditions under which such a dead zone might form and what its radial and vertical extent might be. Recently, a number of numerical studies, pioneered by Fleming & Stone (2003), have begun to explore the dynamical consequences of the dead zone model Fromang & Papaloizou (2006). Turner et al. (2007) have developed an interesting coupled chemical and magnetohydrodynamical (MHD) model in which the dead zone disappears because of vertical mixing of ionized gas to the midplane. In their picture, the dead zone is absent in the sense that large scale magnetic fields with positive Maxwell stress,  $\langle -B_r B_\phi \rangle$ , form in the midplane and transport significant amounts of angular momentum even though the midplane is still MRI stable.

Aside from acting as a conduit for material flowing onto the protostar via accretion, protoplanetary disk midplanes are also the sites of planet formation. One of the outstanding issues in planet formation is the collection of micron-sized dust into planetesimals, rocky objects of order 1 km in size. In this context, turbulent fluid motions more general than the correlated fluctuations that drive accretion become very important. This is because drag forces couple the dust and gas. Fully MRI-active simulations, Johansen & Klahr (2005) find preferential concentration of dust in turbulent over-pressures. However, these same turbulent motions increase the velocity dispersion of the dust grains, possibly leading to destructive collisions. The dust-gas coupling can drive strong instability and clumping (Youdin & Johansen 2007; Johansen & Youdin 2007), which, in combination with MRI turbulence, allows direct formation of planetesimals by gravitational instability (Johansen et al. 2007). Together, these results suggest that turbulence plays a complex role in planetesimal formation. As a first step to considering more complex dust-gas models including dead zones, it is critical to characterize the fluid motions in the MRI-stable midplane.

Here, we address two specific questions about the fluid motions in dead zones: do coherent, two-dimensional (2D) vortices form in dead zones? And, what are the wave-like

motions seen in our previously published models of dead zone dynamics (e.g. Oishi et al. 2007)? Vortices have been studied both for their ability to drive purely hydrodynamic accretion Umurhan & Regev (2004) and their ability to trap dust particles and thus act as sites of enhanced planetesimal formation (Bracco et al. 1999; Johansen et al. 2004). Johnson & Gammie (2005b, hereafter JG05) studied vortex dynamics in a 2D, compressible, shearing sheet model and concluded that random vorticity perturbations do form coherent large-scale vortices, but that energy in such structures decays away as  $t^{-0.5}$ . They also suggested that turbulent overshoot from the active layers might provide a vorticity source at the midplane. Using three-dimensional (3D), compressible but unstratified simulations, Shen et al. (2006) showed that small amplitude vortices are unstable to elliptical instabilities (Kerswell 2002) and that finite-amplitude trailing waves are torn apart by a Kelvin-Helmholtz like instability before they have a chance to form coherent vortices. The anelastic simulations of Barranco & Marcus (2005) show large, coherent vortices forming at 1–3  $H$  from the midplane, where  $H$  is the disk scale height. This unusual and quite unexpected result suggests that stratification plays an important role in disk vortex dynamics. Because our time-steps are Courant-limited by the Alfvén velocity, we restrict our domain to  $|z| < 2H$  to avoid low-density regions with extremely high Alfvén speeds. Nonetheless, we study the effect of stratification on the flow inside and outside of the dead zone with the goal of understanding if MRI turbulence in active layers can sustain vortices.

In section 2 we briefly describe our numerical techniques and how we tested them, while section 3 contains the results of our 3D simulations, and section 4 reviews aspects of vortex dynamics and presents relevant 2D simulations. Finally, we discuss our results and present conclusions in section 5.

## 2. Numerical Method

### 2.1. Model Description

We use the Pencil Code (Brandenburg & Dobler 2002) to solve the resistive MHD equations in the vertically stratified, shearing box limit (Hawley et al. 1995).

All models are 3D, isothermal, non-ideal MHD, except for one ideal MHD control run, and one non-ideal, non-isothermal run (see section 3.3.1). They are run on a domain of  $1H \times 4H \times 4H$ , where  $H$  is the disk scale height. The numerical method is stabilized with sixth-order hyperviscosity, hyperresistivity, and a hyperdiffusive operator on the density as described in Oishi et al. (2007). All the models are initialized with a MRI unstable zero-net flux initial magnetic field given by  $B_z(x) = B_0 \sin(2\pi x/L_x)$  with initial plasma

$\beta = 2\mu_0 P_g / B_0^2 = 400$ . The domain has periodic boundary conditions in  $y$  and  $z$ , and shearing periodic boundaries in  $x$ .

The non-ideal models use one of two  $z$ -dependent resistivity profiles. One is motivated by balancing cosmic ray-ionization to a critical depth in column density given by Fleming & Stone (2003). These models were previously described in Oishi et al. (2007) and are hereafter referred to as “FS runs”. These models were run with cubical zones of size 32 and 64 zones per scale height. Unless otherwise noted, we use a resolution of 64 zones per scale height for the FS runs. The second profile, described below, uses hyperbolic tangent functions and models using it were run with 32 zones per scale height.

## 2.2. Hyperbolic Tangent Resistivity Profile

This alternate profile offers a sharper transition between active and dead zones than the FS profile, and allows the thickness of the dead zone to be controlled independently from its depth. Though simpler, it is less physically motivated than the FS profile. The profile is given by

$$\eta(z) = \frac{\eta_0}{2} \left( \tanh \left( \frac{z + z_0}{\Delta z} \right) - \tanh \left( \frac{z - z_0}{\Delta z} \right) \right) \quad (1)$$

where  $\eta_0$  is the midplane resistivity,  $z_0$  is the transition height and  $\Delta z$  is the width of the transition region, set in this work to  $\Delta z = 5dx$ , where grid zones have size  $dx$ . We set  $\eta_0 = 1.67 \times 10^{-5}$ , corresponding to magnetic Reynolds number  $Re_M = c_s^2 / (\eta_{mid} \Omega) = 30$  at  $z < |z_0|$ . This gives all our tanh models the same value of  $Re_M$  in the dead zone as our fiducial FS run has at  $z = 0$ .

The Maxwell stresses as a function of height for both sets of profiles are given in Figure 1. The figure emphasizes the main utility of the tanh profile: because the dead zone resistivity is independent of its size, we can study larger dead zones at a given resolution.

## 2.3. Tests

In the numerical study of non-axisymmetric perturbations in disks, a series of test problems are becoming standard. The vortical and non-vortical shearing waves have closed analytic solutions (in the former case, a WKB approximation) derived by Johnson & Gammie (2005a). These waves have been used by JG05 to test a code derived from ZEUS (Stone & Norman 1992) and the higher-order Godunov code ATHENA (Shen et al. 2006). Aside from providing an analytic test solution for comparison, the incompressible wave is particularly

useful for determining the amount of aliasing present in the numerical scheme. As a wave swings from leading to trailing, it wraps toward axisymmetry. However, in doing so the number of zones resolving the wave must drop. When the number of zones resolving each wavelength drops below some threshold, the code may unphysically transfer (“alias”) power from the trailing wave into a new leading wave that will again swing amplify. This danger is highlighted by both Umurhan & Regev (2004) and Shen et al. (2006), as such power may spuriously drive coherent vortices and angular momentum transport.

The Pencil Code uses spatially-centered finite differences and Runge-Kutta timestepping, meaning that its discretization lacks any formal algorithmic viscosity. Thus, it should perform well on this test. Ultimately, however, this property works against the code: without an explicit viscous term, it does not dissipate energy that moves to smaller scales, where an unphysical buildup occurs. In this sense, the shearing waves mimic the effect of a turbulent cascade: as time progresses,  $k_x(t)$  decreases and the waves become less and less resolved. This is not a turbulent cascade of course, but the code is nonetheless forced to resolve smaller and smaller structures, leading eventually to a crash. To avoid this in these tests, as in our actual runs, we use a sixth-order hyperviscosity scaled by  $\nu_6$  for stability, setting the hyperviscous Reynolds number at the grid scale  $Re_6 = udx^5/\nu_6 \simeq 1$ , where  $u$  is the maximum velocity on the grid.

Figure 2 shows the incompressible shearing wave for runs with resolution  $N = 64, 128, 256$ , demonstrating the ability of the Pencil code to accurately reproduce the analytic solution. The aliasing time in terms of the orbital frequency is (Shen et al. 2006)

$$t_{alias}\Omega_0 = \frac{n}{q} \left( \frac{N_x}{n_y} - \frac{k_{x0}}{k_y} \right), \quad (2)$$

where  $n$  is an integer,  $q = d \ln \Omega_0 / d \ln r$  is the shear parameter, and  $n_y = k_y L_y / 2\pi$  is the dimensionless azimuthal wavenumber of the wave. The oscillations around  $t = 20$  appear to be small amplitude sound waves present in our compressible solution but not in the incompressible analytic solution.

In Figure 2, the  $N = 64, 128$ , and 256 models run to  $t\Omega_0 = 100$ , where  $\Omega_0$  is the local orbital frequency. This is well beyond the expected aliasing time  $t_{alias}\Omega_0 \simeq 45.3n$  for  $N_x = 128$  and  $90.6n$  for  $N_x = 256$ . The figure makes an interesting point: aliasing does indeed occur for  $64^2$ , but because the hyperviscosity is a strongly non-linear function of resolution, the spurious energy injected by aliasing becomes trivial before the first  $128^2$  aliasing time. Even at  $64^2$ , each successive aliased wave has less power, suggesting that sustained vortex activity is not likely to be powered by this numerical effect for long times. There is no aliasing at all at  $128^2$  and  $256^2$  resolutions, because the hyperviscosity damps the signal to machine precision before the first aliasing time. We have additionally performed a

convergence test using resolutions of 64, 128, and 256. Using hyperviscosity, the average error over  $t\Omega < 10$  reaches a constant value at  $128^2$  and does not further converge. However, when we stabilize the algorithm using a physical Laplacian viscosity instead of hyperviscosity,  $\mathbf{f}_\nu = \nu \nabla^2 \mathbf{u}$ , the error converges at roughly  $\sim N^{-1.6}$  where  $N$  is the resolution. We also consider the compressible shearing wave. Figure 3 demonstrates the code’s ability to resolve the wave with small error to late times with moderate resolution.

Finally, we successfully tested against the 3D, hydrodynamic, non-linear solution of the shearing box equations derived by Balbus & Hawley (2006). Figure 4 shows the kinetic energy of the wave as function of time. In this test, as in the others, the wavenumber drops, so that at larger times the error necessarily grows.

The incompressible shear wave test gives us a strict metric for aliasing: for the lowest resolution, we used  $H = 64dx$ , and saw trivial amounts of aliasing. Doubling the resolution to  $H = 128dx$ , we see no aliasing. Because the amount of vorticity *increases* in our MHD simulations when we increase the resolution from  $H = 32dx$  to  $64dx$  (see figure 5), we are confident that any sustained vorticity in our MHD simulations does not come from numerical aliasing, and that the code accurately tracks any vortical motions present.

### 3. Results

The excitation and saturation of the MRI occur by  $t/t_{orb} = 5$  and the dead zone is clearly defined by orbit  $\sim 10$  (see section 3.3 for details). Here, we will restrict our analysis to times later than 25 orbits in order to avoid transients. Figure 6 shows time series of vorticity ( $\omega = \nabla \times \mathbf{u}$ ), and kinetic and magnetic energies. Although the saturated kinetic energy drops by over an order of magnitude between the  $Re_M = \infty$  and the  $Re_M = 3$  models, the vorticity only drops by a factor of a few. This can be explained by the presence of residual vorticity in the dead zone.

#### 3.1. Vorticity and Flow Dimensionality

The MRI produces significant amounts of vorticity, much of which is retained when a dead zone is introduced. Here, we investigate whether or not this vorticity can coalesce into coherent vortices that could be significant as a natural environment in which to trap dust and thus accelerate protoplanet formation.

In a thin accretion disk, the vertical gravitational acceleration is given by

$$\mathbf{g} = -\Omega^2 z \hat{\mathbf{z}}, \quad (3)$$

where  $\Omega$  is the orbital frequency. In the local approximation, we take  $\Omega_0 = \Omega(R)$  where  $R$  is the assumed central radius of the shearing box. For an isothermal disk in hydrostatic equilibrium, the Brunt-Väisälä frequency of buoyant vertical oscillation is

$$N^2 = -\frac{\mathbf{g}}{\rho} \frac{\partial \rho}{\partial z} = \frac{\Omega_0^2 z^2}{H^2}. \quad (4)$$

We can diagnose how stratified the flow is by comparing the vertical component of the vorticity  $\omega_z$  to the Brunt-Väisälä frequency  $N$  in a version of the internal Froude number, (e.g., Barranco & Marcus 2005)

$$\text{Fr} = \omega_z / (2N). \quad (5)$$

$N$  vanishes at the midplane, and thus  $\text{Fr}$  formally diverges as  $z \rightarrow 0$ . Nonetheless,  $\text{Fr}$  provides a useful diagnostic for the degree of stratification in the flow: when  $\text{Fr} < 1$ , internal gravity waves rapidly homogenize vertical disturbances in the vortex, so the system is strongly stratified, and acts effectively as a 2D flow in which energy cascades to larger scales, similarly to the Earth’s atmosphere. Thus,  $\text{Fr}$  is an effective measure of the dimensionality of a vortex in the disk plane.

Previous results show rapid vortex growth in purely 2D systems integrated over  $z$  (Umurhan & Regev 2004; Johnson & Gammie 2005b), and at  $Fr < 1$  in 3D stratified systems (Barranco & Marcus 2005). Figure 7 shows the vertical behavior of  $Fr$  in our FS models. All but one of our simulations are purely isothermal, with  $P = c_s^2 \rho$ , so gravity waves themselves are excluded. However, because the basic dynamical properties of the MRI are not very sensitive to the equation of state (Stone et al. 1996), we do not expect that including gravity waves will change the  $Fr$  profile. We confirm this expectation in figure 7, which also includes our control  $Re_M = 30$  run with a non-isothermal,  $\gamma = 5/3$  ideal gas equation of state (see section 3.3.1 for more details). The  $Fr$  profile is roughly similar to the run with isothermal  $Re_M = 30$ .

In our ideal MHD run the flow is effectively 3D through almost the entire domain—the MRI is a strong enough vorticity source to overwhelm the homogenizing effect of vertical oscillations almost everywhere. On the other hand, Figure 7 suggests that the dead zone models have an effectively 2D flow at nearly all heights, most particularly in the dead zone of the  $Re_M = 3$  model. Near the midplane,  $Fr$  diverges, as the stratification there goes to zero, so we would expect the very near midplane region to act as a 3D flow, consistent with the Barranco & Marcus (2005) results showing disappearance of their imposed vortices in that region.

However, Figure 8 shows that no vortices form in either the dead or the active zone. In the dead zone, the vorticity remains confined to elongated, nearly axisymmetric bands. In fact, no difference is seen in  $\omega_z$  between heights within the dead zone—only between dead and active zones. Thus, our results combined with Shen et al. (2006) and Barranco & Marcus (2005), show that even in the presence of a vorticity source such as active zones, stratification is necessary but insufficient to produce vortices.

Table 1 shows the distribution of enstrophy among  $x, y$ , and  $z$  components for FS models and the ideal MRI run. A strongly two-dimensional flow shows a preferred direction (Brandenburg et al. 1995). The ideal MRI run and the active zones of the FS models agree well with an isotropic distribution of vorticity. The dead zones show a strong preference for the  $y$  direction, indicating a circulation in the  $x - z$  plane, as indeed images bear out (see below). The coherent anticyclonic vortices we set out to investigate would have shown a strong  $z$  component.

Figure 9 shows the components of velocity dispersion for each of the FS runs as a function of time, computed separately inside and outside of the dead zone. The  $z$  component of velocity dominates within the dead zone, while outside of it, it is a factor of a few smaller than the others. (Note that the oscillation in the dead zone velocities is real, but the plot was made with relatively crude time resolution,  $\delta t = 0.5t_{orb}$  and some aliasing from higher frequency signals is certainly present.) The dead zone motion is clearly not dominated by horizontal flows.

### 3.2. Morphology and velocity vectors

Figure 10 shows images of density overlaid with velocity vectors for the midplane (the  $x-y$  plane at  $z = 0$ ) and Figure 11 the  $x-z$  plane at  $y = 0$  for each of the FS runs. In the dead zone midplanes (the right three panels), compressive waves dominate the velocity field: velocity vectors lie almost entirely orthogonal to the density striations in the  $x-y$  plane. However, in the  $x-z$  plane, inertial mode signatures appear: the velocity is dominated by the  $z$  component, traveling up and down in well defined vertical bands.

The dead zone shows ordered  $u_z$  alternating between positive and negative values across the dead zone that become more pronounced as  $Re_M$  decreases (Fig. 11, right three panels). This suggests that the vertical oscillations are at  $\theta = 0$ , with energy transport from gravity waves purely vertical between the active zones and the midplane. This is in stark contrast to the fully MRI-active case. Near its midplane, there are no well-defined vertical oscillations, and the  $Re_M = 100$  model does not show nearly as well-ordered motion as the larger dead



zone models. This is perhaps not surprising given that the fastest growing MRI mode has a growth rate  $q_{MRI} \sim \Omega_0$ , which is greater than  $N$  until around a scale height.

### 3.3. Wave Modes

The MRI is not operating in the densest parts of the disk in our dead zone models, so we expect that the motions excited in this region will take the form of linear wave modes stochastically excited by the active zone turbulence. The following analysis is motivated by the low-frequency oscillation in the volume-averaged kinetic energy most clearly shown in the  $Re_M = 3$  data between  $60 < t < 100$  in Figure 6. Fourier analysis of this kinetic energy time series for runs with a dead zone show a clear peak in frequency space that shifts slightly to lower frequency with increasing dead zone size, suggesting the presence of a large amplitude coherent oscillation in these runs.

In order to better understand these dead zone oscillations, we take temporal power spectra of the radial and vertical velocity components  $u_x$ , and  $u_z$ , and the density perturbation  $\delta\rho = \rho(x, y, z) - \rho_0(z)$ . Arras et al. (2006) and Brandenburg (2005) used similar methods to diagnose global modes of oscillation in fully magnetorotationally turbulent disks. The former were able to isolate acoustic and inertial oscillations. However, the latter found no clear wave signatures for MRI turbulence, though they did recover acoustic and inertial modes for forced hydrodynamic turbulence in a shearing box.

Figure 12 shows spectra computed by taking an FFT of a time series of each variable averaged in the  $y$ -direction at every  $(x, z)$  point on the grid of our low resolution model. The resulting power spectra were then averaged to raise signal-to-noise. Azimuthal averaging allows us to eliminate much of the MRI power in the active zones (Arras et al. 2006), though this may not be a significant source in some of our larger dead zone models. The dominant peak in all variables at  $\varpi_{max} \simeq 0.23\Omega_0$  shifts only very slightly, to lower frequency, as the dead zone is made thicker by a factor of two in the tanh runs. This suggests that the vertical thickness of the dead zone is not setting the oscillation frequency. We have also determined that this characteristic frequency is unaffected by the radial ( $x$ ) extent of the box by running the  $Re_M = 30$  model with  $L_x = 2$  and confirming that the oscillation frequency is unchanged.

Because the box is periodic, standing oscillations can be excited, with discrete frequencies. The lowest frequency acoustic mode is in the vertical direction and has a frequency  $\varpi \simeq c_s 2\pi/L_z = 1.11\Omega_0$ , which is clearly larger than  $\varpi_{max}$ . The isothermal equation of state used in these models precludes gravity waves (which would also have  $\varpi < \Omega_0$ ), and so we tentatively identify them as an inertial oscillation. Furthermore, the small shift seen in the

tanh runs as the dead zone thickness increases is actually to *lower* frequency, while a higher boundary would drive internal oscillations at a *higher* frequency (see Eq. 4) .

### 3.3.1. *Non-isothermal models and Buoyancy Forces*

The low frequency of these oscillations is suggestive of a gravity mode. However, these runs are strictly isothermal,  $P = c_s^2 \rho$  with  $c_s$  constant everywhere, precluding buoyant responses and thus gravity waves.

Recently, Bai & Goodman (2009) noted that isothermal equations of state might spuriously enhance vertical mixing, as buoyant forces can inhibit vertical mixing. Likewise, the lack of buoyancy in our isothermal models may artificially enhance both the residual transport at the midplane and the coherent oscillations. In order to understand the effect of isothermality on these issues, we ran a single model at 32 zones per scale height including an ideal gas equation of state  $P = \rho kT/\mu$  and an entropy equation,

$$\rho T \left( \frac{\partial s}{\partial t} + \mathbf{u} \cdot \nabla s + u_y^0 \frac{\partial s}{\partial y} \right) = \eta(z) \mu_0 \mathbf{j}^2 + \zeta \rho (\nabla \cdot \mathbf{u})^2 + \kappa_6 \nabla^6 s, \quad (6)$$

where  $\kappa_6$  is a hyperdiffusivity of entropy,  $u_y^0 = -3/2\Omega x$  is the Keplerian velocity profile,  $\Omega$  is the rotation rate of the shearing box, and all other symbols have their usual meanings. The entropy equation includes resistive and shock heating but not heating from the hyperdiffusivities (these terms are small, and do not significantly contribute to the thermal balance). We chose a ratio of specific heats  $\gamma = 5/3$ .

The boundary conditions on this run as on the others are periodic in all directions, which precludes the escape of heat. We choose this rather unrealistic setup to directly compare with our isothermal simulations, in order to demonstrate that our results are not due to the lack of buoyancy in the isothermal case. Because of the turbulent heating, the total energy in the box increases compared to the isothermal case. Although the turbulence is strongest in the surface layers, there is no temperature inversion in the vertical direction: the midplane remains hotter than the surface. The disk quasi-statically adjusts to new equilibrium density and pressure profiles as the energy increases. While these profiles are somewhat different from the standard Gaussian density profile expected for accretion disks with linear  $z$ -gravity profiles, Figure 5 shows that the main result of this difference is a factor  $\sim 2$  increase in magnetic energy, and a factor  $\sim 1.8$  increase in kinetic energy.

The overall morphology of the flow is roughly similar to the isothermal model, with a reduced amplitude of motion in the dead zone but a similar large-scale structure. The stress profile across the dead zone is narrower but deeper in the ideal gas run than the isothermal

one because of the pressure confinement caused by turbulent heating in a periodic box absent cooling. We directly compare the Maxwell and Reynolds stresses for isothermal (labeled  $\gamma = 1$ ) and ideal gas ( $\gamma = 5/3$ ) in Figure 13. We find that inclusion of the buoyant forces reduces the amplitude of the vertical motions and increases their characteristic frequency to  $\varpi_{max} \simeq 0.5\Omega_0$ , still well below the first acoustic mode, as shown in Figure 14. However, the motions are not suppressed, even in this model in which turbulent heating is not at all balanced by cooling. A real disk in which cooling is allowed will fall between the limits of the isothermal model and this heating only model. Therefore, we argue that the dead zone motions represent a physical phenomenon even in the presence of buoyancy forces.

#### 4. Midplane Vortex Dynamics

We see no vortices in our simulations. We must establish that this is a physical result, and not due to insufficient resolution. JG05 demonstrate that sufficient numerical resolution is necessary to sustain kinetic energy and angular momentum transport from vortices. In their 2D simulations, they find  $128dx/H$  to be the critical value, raising the question of whether vortices can form in 2D at our resolutions ( $32dx/H$  or  $64dx/H$ )? Furthermore, the typical radial size scale of a vortex in their simulations is roughly  $H$ , the entire width of our box. Can vortices form in such cramped quarters?

##### 4.1. Two-Dimensional Vortex Dynamics

In order to clarify these issues, we ran four sets of 2D hydrodynamic simulations. First, we studied resolution. A comparison between Figure 2 and Figure 1 of JG05 shows that the sixth-order Pencil Code is significantly less diffusive than their second-order, Zeus-derived method, suggesting that we might be able to see sustained vortex activity at lower resolution. Therefore we ran a set of models using their domain with size  $L_x = L_y = 4H$  at resolutions of  $(16, 32, 64)dx/H$ , all with Gaussian random velocity perturbations with the same initial perturbation amplitude,  $\sigma = 0.8c_s$ . Figure 15 shows the kinetic energy and  $\alpha$ -parameter,  $\alpha = \langle \Sigma u_x u_y \rangle$  for 2D. This Figure demonstrates clear convergence in these integrated quantities at  $32dx/H$ .

Next, we turn to the question of domain size. JG05 use a domain four times larger in radial extent than we do in our 3D simulations. Could this inhibit vortex formation in our MHD runs? To test this, we ran a set of 2D hydrodynamic models with the same domain as the midplane of our 3D simulations,  $L_x = 1H$  and  $L_y = 4H$ , again with resolutions of

$(16, 32, 64)dx/H$ , seeded with perturbations of magnitude  $\sigma = 0.8c_s$ . Figure 16 shows that vortex morphology is largely similar in both domains at three times, though there are more vortices present in the square domain.

Figure 17 shows the resulting energy and  $\alpha$ . Although the results are not as well converged as in the square domain, there is still evidence for vortex activity with lifetimes clearly greater than the MRI growth time  $\tau_{\text{MRI}} \sim \Omega$  at a resolution of  $32dx/H$ .

What, then, is the reason we do not see vortex activity in the 3D dead zone simulations? We have argued that dimensionality is not the limiting factor, as regions with lower Froude number that are more effectively 2D do not show more vorticity. It also appears clear that the 2D vortex activity found in previous simulations can be reproduced on domains like ours at the resolutions we use in our MHD runs, so resolution and grid size are also not limiting. Rather, the discriminant appears simply to be the *strength* of perturbations required to trigger long-lived vortices. We ran a third set of 2D hydrodynamic simulations, this time at a fixed resolution of  $32dx/H$ , but with decreasing velocity perturbation magnitudes  $\sigma = 0.8c_s, 0.5c_s$ , and  $0.1c_s$ . Figure 18 shows that below  $\sigma = 0.8$ , the kinetic energy and  $\alpha$  drop precipitously after only a few orbits. (Note that we keep the domain size fixed at  $L_x = 1H, L_y = 4H$ , unlike in the tests of JG05, in which the domain size was scaled linearly with the strength of the velocity dispersion.) We conclude that *compressible* vortices require strong  $\sigma = 0.8c_s$  initial perturbations in order to survive for many orbits.

Umurhan & Regev (2004) see perturbation energy sustained essentially indefinitely for  $Re = \infty$  and decaying away only very slowly for  $Re = 50000$ , but their model is incompressible. They show this approximation to be rigorously valid for the small length scales they consider. However, interestingly, they find that the perturbation energy saturates at roughly  $\lesssim 10^{-2}E_{\text{shear}}$ , where  $E_{\text{shear}}$  is the energy in the shear. They define the turbulent intensity of an incompressible shear flow as

$$\varepsilon_0 = \frac{\int u^2 dx dy}{\int u_{sh}^2 dx dy} \lesssim 10^{-2}, \quad (7)$$

with  $u$  the disturbance velocity and  $u_{sh}$  the shear velocity. We write  $u_{sh} = q\Omega x$ , integrate for the Keplerian case  $q = -3/2$ , and use our definition of (thermal) scale height  $H = 2c_s/\Omega$  to arrive at

$$\langle \text{Ma}^2 \rangle = \frac{\sigma^2}{c_s^2} = \frac{3}{8}\varepsilon_0 \left( \frac{L_x}{H} \right)^2, \quad (8)$$

with  $\langle \text{Ma}^2 \rangle^{0.5} = \text{Ma}_{rms}$  the RMS Mach number. Using their saturation value, this gives  $\text{Ma}_{rms} \sim 0.06(L_x/H)$ , or about 0.06 over a domain of  $H$ . This is an order of magnitude below the levels necessary to incite vortices on the larger scales that we simulate in which compression becomes important. If we assume that small scale, non-linear, transient growth

instability scales with Reynolds number as found by Lesur & Longaretti (2005), not only is the incompressible, small-scale, transient growth irrelevant for angular momentum transport, its saturation level is so small that larger scale vortices in the compressible regime will not form at all.

## 4.2. Long-lived axisymmetric structures

Recently, Johansen et al. (2009) reported the existence of long-lived axisymmetric zonal flows in MRI turbulence, provided the radial width of the box is larger than  $\sim 1H$ . These structures result from an inverse cascade of magnetic energy to the largest scales present in the box. This energy drives a large scale Maxwell stress, which in concert with the Coriolis force enforces the zonal flow. The end result are long-lived ( $\sim 10$ s of orbits) pressure and density fluctuations. It is easy to imagine that these complex structures could have significant influence on motions in the dead zones, assuming there is sufficient magnetic energy to launch the zonal flows in the first place. Figure 1 implies that this criterion is unlikely to be met: even in the moderate sized dead zone models (e.g.,  $Re_M = 30$  and  $z_0 = 1$ ), the total Maxwell stress is many orders of magnitude lower than that in the MRI active zones. However, given that Johansen et al. (2009) demonstrate that the zonal flows are subtle, stochastically driven, and non-linear, we find such a crude estimate to be unsatisfactory.

Therefore, we re-ran our  $Re_M = 30$  FS model with a radially-enlarged domain, running from  $-H < x < H$ . By averaging  $\rho$  over the entire  $y - z$  domain, including both active and dead zones, we recover the reported long-lived axisymmetric structures. Nevertheless, our results remain robust: there is no vortex formation, and figure 19 demonstrates that the midplane oscillations are quite similar between the larger domain and our fiducial case.

## 5. Discussion

We find a complete lack of coherent anticyclonic vortices in all of our stratified local simulations of dead zones, despite the presence of a vorticity source in the form of active zones. While our experiments do not tell us exactly what happens, it appears that even if the midplane were a pure 2D layer, large scale vortex formation would not occur because the amplitude of velocity perturbations driven in the dead zone by the active layers is well below that needed. Recent work by Lesur & Papaloizou (2009) suggests that vortices in 3D disks are always parametrically unstable, though the growth rates of such instabilities can be very slow. Even in the presence of an active vorticity source, though, we find no vortex

formation.

Our simulations cover a smaller range of  $z$  than Barranco & Marcus (2005), and it is possible that the increased stratification present at higher  $z$  may change our results. To strengthen the results presented here, direct comparison with Barranco & Marcus (2005) including compressibility would be quite enlightening. Furthermore, almost all of our simulations use an isothermal relation for pressure and density. This forces density gradients and pressure gradients to coincide, eliminating the baroclinic term driving the vortex formation from breaking gravity waves in Barranco & Marcus (2005). Relaxing this requirement in our simulations may aid vortex formation at higher scale heights though our one adiabatic model without cooling did not show vortex formation either.

However, we do find a large-scale, axisymmetric oscillation about the midplane in all dead zone models. This oscillation carries nearly all the kinetic energy of the dead zone. We are unable to associate it with a normal mode using a simple linear dispersion relation. A more detailed analysis including the effects of continuous stratification could shed considerable light on the situation. Regardless of such details, the low frequency (less than  $\Omega_0$ ) suggests that the mode will not have much effect on dust sedimentation, which is typically dominated by random fluctuation with correlation times  $\tau_{corr} \simeq 0.15t_{orb}$ , corresponding to frequencies  $\simeq 7\Omega_0$  (Fromang & Papaloizou 2006). It could, in principle, cause a warp in the dust layer, which in turn could affect the gravitational stability (Goldreich & Ward 1973; Johansen et al. 2007). Such phenomena can only be examined with a combined treatment of dust, self-gravity, and a dead zone, which we defer to future work.

Finally, global dynamics may significantly alter vortex formation properties. A real protoplanetary disk is thin and quasi-2D for horizontal scales greater than the scale height. It is quite possible that robust, anticyclonic vortices may form within a disk, but our results suggest that a local mechanism is not responsible. The baroclinic instability (Klahr & Bodenheimer 2003; Petersen et al. 2007a,b) remains a candidate for forming such large scale vortices.

JSO would like to thank the Hausdorff Research Institute for Mathematics at Universität Bonn, where a considerable portion of this work was completed, for their hospitality and financial support. J. Hawley, K. Menou, and P. Arras made useful suggestions on an early version of this manuscript. Computations were performed at the Parallel Computing Facility of AMNH and the Cray XT3 “Big Ben” at the Pittsburgh Supercomputing Center, the latter of which is supported by the National Science Foundation. M-MML was partially supported by NASA Origins of Solar Systems grant NNX07AI74G and by NSF grant AST08-35734.

## REFERENCES

- Arras, P., Blaes, O., & Turner, N. J. 2006, *ApJ*, 645, L65
- Bai, X.-N., & Goodman, J. 2009, arXiv:0904.1240
- Balbus, S. A., & Hawley, J. F. 2006, *ApJ*, 652, 1020
- Barranco, J. A., & Marcus, P. S. 2005, *ApJ*, 623, 1157
- Blaes, O. M., & Balbus, S. A. 1994, *ApJ*, 421, 163
- Bracco, A., Chavanis, P. H., Provenzale, A., & Spiegel, E. A. 1999, *Physics of Fluids*, 11, 2280
- Brandenburg, A. 2005, *Astronomische Nachrichten*, 326, 787
- Brandenburg, A., & Dobler, W. 2002, *Comput. Phys. Comm.*, 147, 471
- Brandenburg, A., Nordlund, Å., Stein, R. F., & Torkelsson, U. 1995, *ApJ*, 446, 741
- Gammie, C. F. 1996, *ApJ*, 457, 355
- Fleming, T., & Stone, J. M. 2003, *ApJ*, 585, 908
- Fromang, S., & Papaloizou, J. 2006, *A&A*, 452, 751
- Goldreich, P., & Ward, W. R. 1973, *ApJ*, 183, 1051
- Hawley, J. F., Gammie, C. F., & Balbus, S. A. 1995, *ApJ*, 440, 742
- Jin, L. 1996, *ApJ*, 457, 798
- Johansen, A., Andersen, A. C., & Brandenburg, A. 2004, *A&A*, 417, 361
- Johansen, A., & Klahr, H. 2005, *ApJ*, 634, 1353
- Johansen, A., Oishi, J. S., Mac Low, M.-M., Klahr, H., Henning, Th., & Youdin, A. 2007 *Nature*, 448, 1022
- Johansen, A., & Youdin, A. 2007, *ApJ*, 662, 627
- Johansen, A., Youdin, A., & Klahr, H. 2009, *ApJ*, 697, 1269
- Johnson, B. M., & Gammie, C. F. 2005a, *ApJ*, 626, 978
- Johnson, B. M., & Gammie, C. F. 2005b, *ApJ*, 635, 149 (JG05)

- Kerswell, R. R. 2002, *Annual Review of Fluid Mechanics*, 34, 83
- Klahr, H. H., & Bodenheimer, P. 2003, *ApJ*, 582, 869
- Lesur, G., & Longaretti, P.-Y. 2005, *A&A*, 444, 25
- Lesur, G., & Papaloizou, J. C. B. 2009, *A&A*, 498, 1
- Oishi, J. S., Mac Low, M.-M., & Menou, K. 2007, *ApJ*, 670, 805
- Petersen, M. R., Julien, K., & Stewart, G. R. 2007, *ApJ*, 658, 1236
- Petersen, M. R., Stewart, G. R., & Julien, K. 2007, *ApJ*, 658, 1252
- Shen, Y., Stone, J. M., & Gardiner, T. A. 2006, *ApJ*, 653, 513
- Stone, J. M., & Norman, M. L. 1992, *ApJS*, 80, 753
- Stone, J. M., Hawley, J. F., Gammie, C. F., & Balbus, S. A., *ApJ*, 463, 656
- Turner, J. S. 1973, *Buoyancy Effects in Fluids*. Cambridge, UK: Cambridge University Press
- Turner, N. J., Sano, T., & Dziourkevitch, N. 2007, *ApJ*, 659, 729
- Umurhan, O. M., & Regev, O. 2004, *A&A*, 427, 855
- Youdin, A., & Johansen, A. 2007, *ApJ*, 662, 613



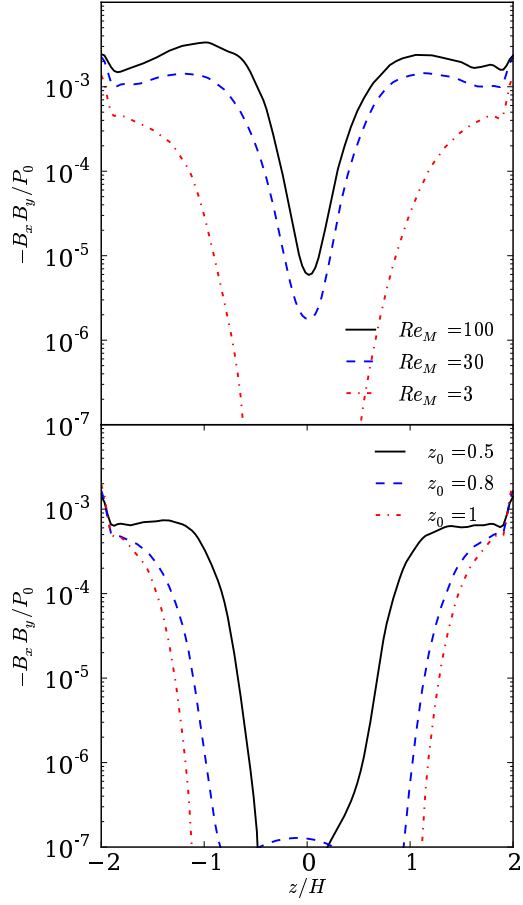


Fig. 1.— Maxwell stress as a function of height  $z$  for three different values of magnetic Reynolds number using the FS profile, and three different transition heights  $z_0$  using the tanh resistivity profile (Eq. 1). At very high  $\eta$  values, the stress is occasionally positive and therefore absent on this plot.

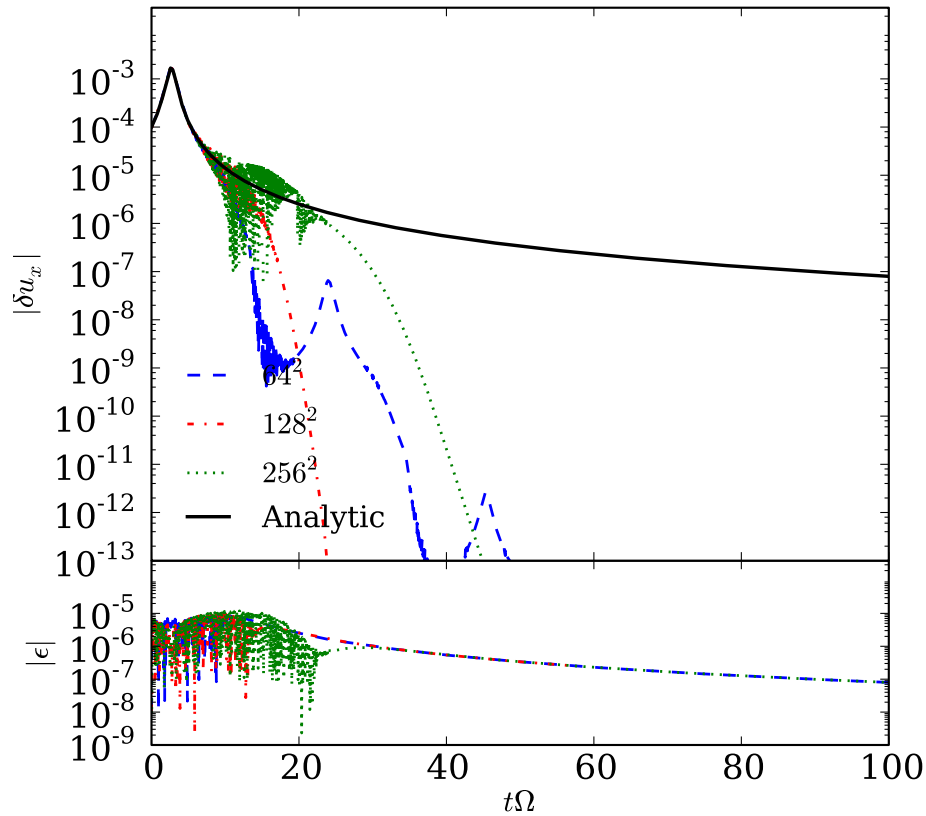


Fig. 2.— Time evolution of the velocity perturbation amplitude  $\delta u_x$  of an incompressible, shearing wave (upper panel) using physical viscosity for resolutions from  $64^2$  to  $128^2$ . The analytic solution is given in black. Aliasing is present in the  $64^2$  solutions but injects only trivial amounts of energy. The lower panel shows absolute value of the error,  $|\epsilon| = |\delta u_x - \delta u_x^{analytic}|$ . Note that this error smoothly asymptotes to the analytic solution as the code hyperviscously damps the wave faster than aliasing can inject spurious energy.

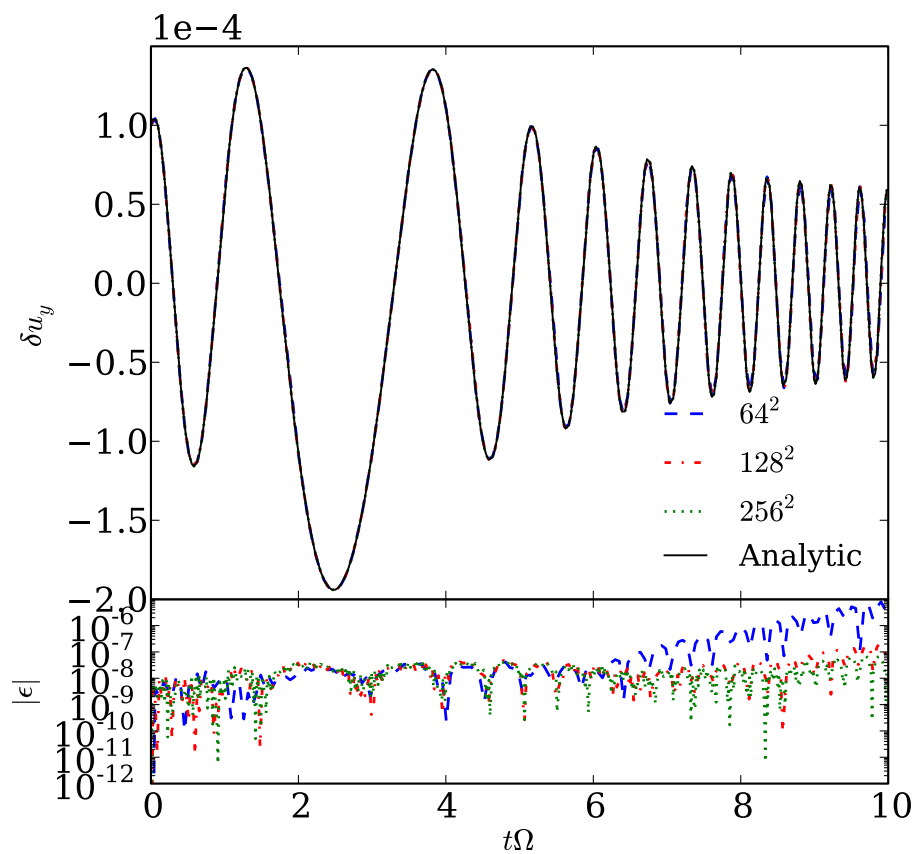


Fig. 3.— Time evolution of the amplitude  $\delta u_y$  of a compressible, shearing wave using hyperviscosity for resolutions from  $32^2$  to  $128^2$ . The analytic solution is given in black. The lower panel shows the absolute value of the error,  $|\epsilon| = |\delta u_y - \delta u_y^{analytic}|$ , between the Pencil Code solution and a numerically integrated solution to the exact parabolic cylinder equation describing the wave.

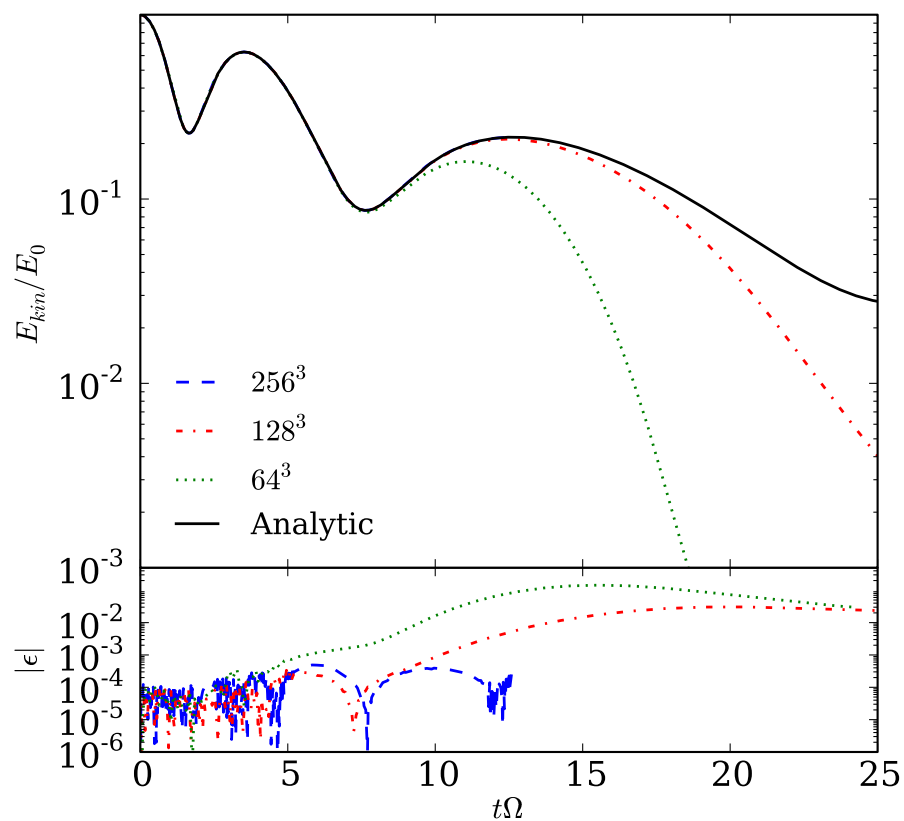


Fig. 4.— Time evolution of the kinetic energy of a 3D, non-linear, incompressible, shearing wave using hyperviscosity for resolutions from  $64^3$  to  $256^3$ . A numerical integration of the exact wave differential equation is given in black and labeled “Analytic”. The lower panel shows absolute value of error,  $|\epsilon| = |E_{kin} - E_{kin}^{analytic}|$

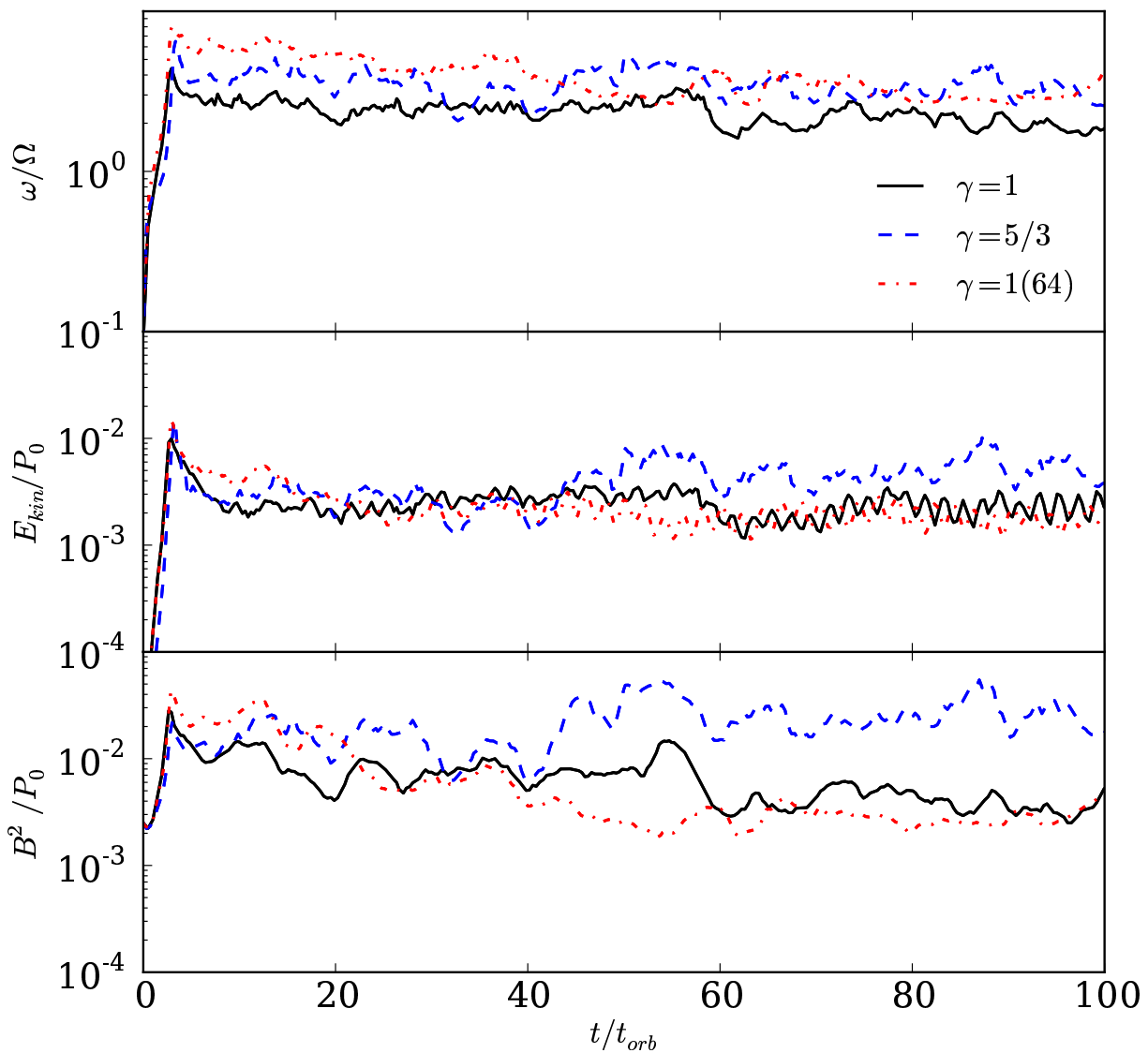


Fig. 5.— From top to bottom: volume averaged vorticity ( $\omega$ ), kinetic, and magnetic energy comparing isothermal and ideal gas  $Re_M = 30$  runs. Isothermal runs at  $H = 64dx$  and  $H = 32dx$  are overplotted. The amount of vorticity increases with increasing resolution.

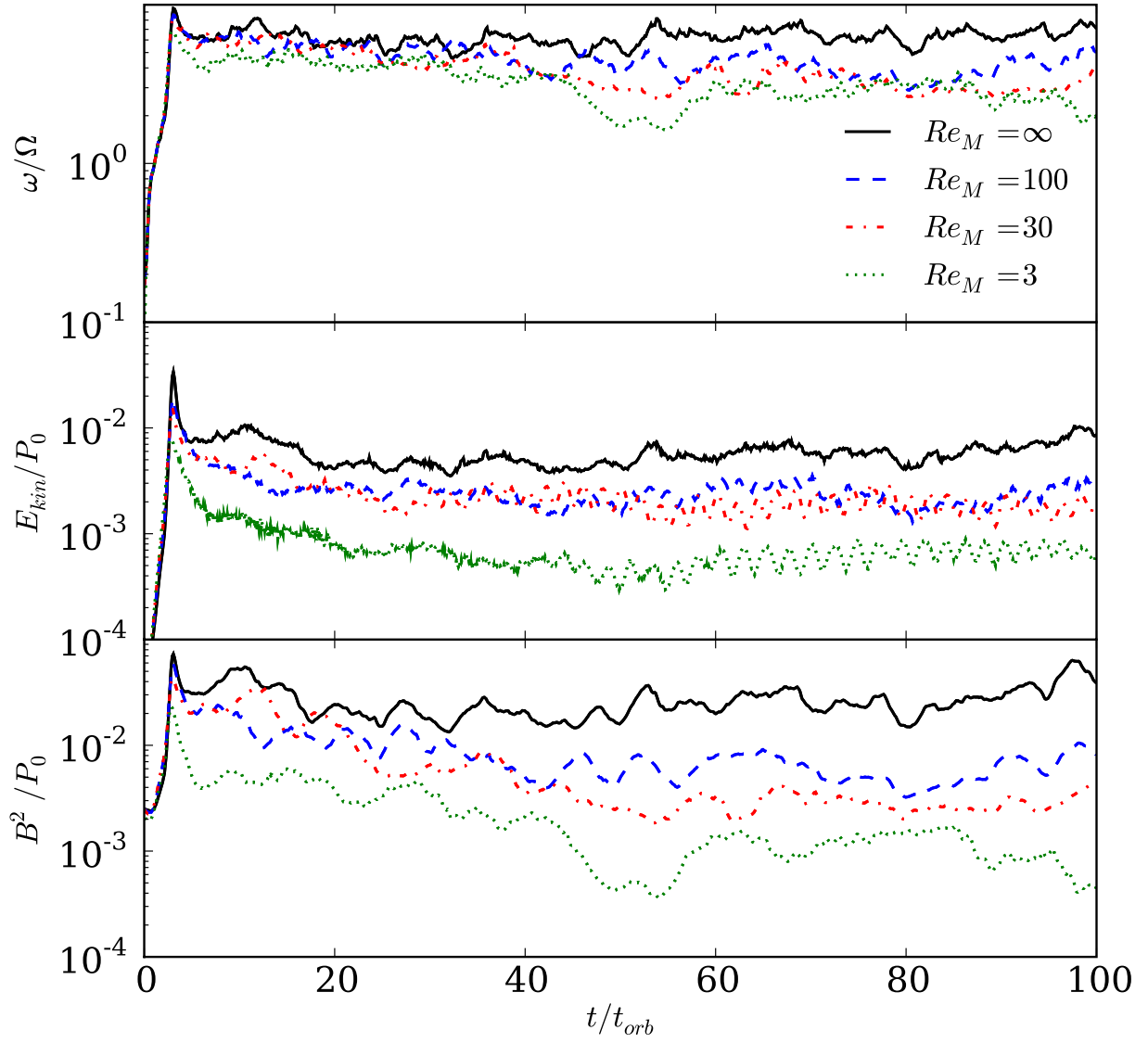


Fig. 6.— Same as figure 5 for each  $H = 64dx$  resolution FS run.

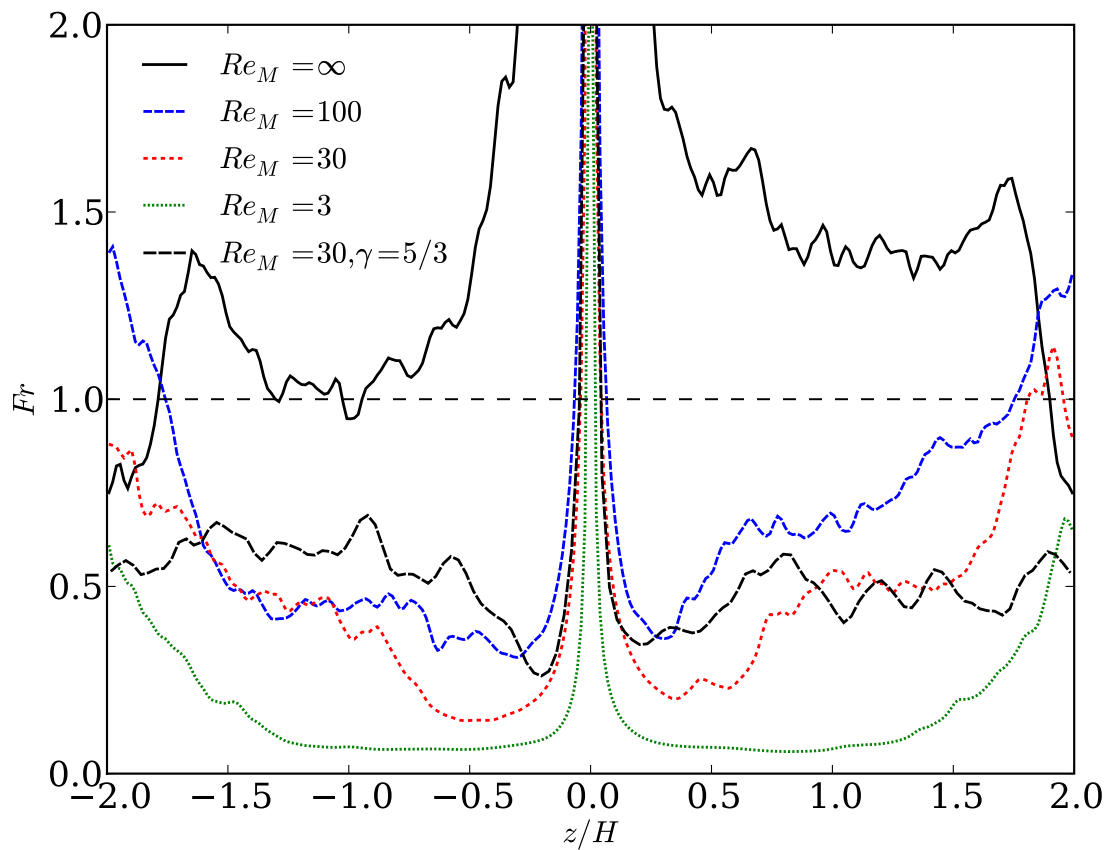


Fig. 7.— Internal Froude number versus height above the midplane for the FS runs. At  $Fr \lesssim 1$ , the flow becomes strongly stratified and effectively two-dimensional for vortices lying in the disk plane.

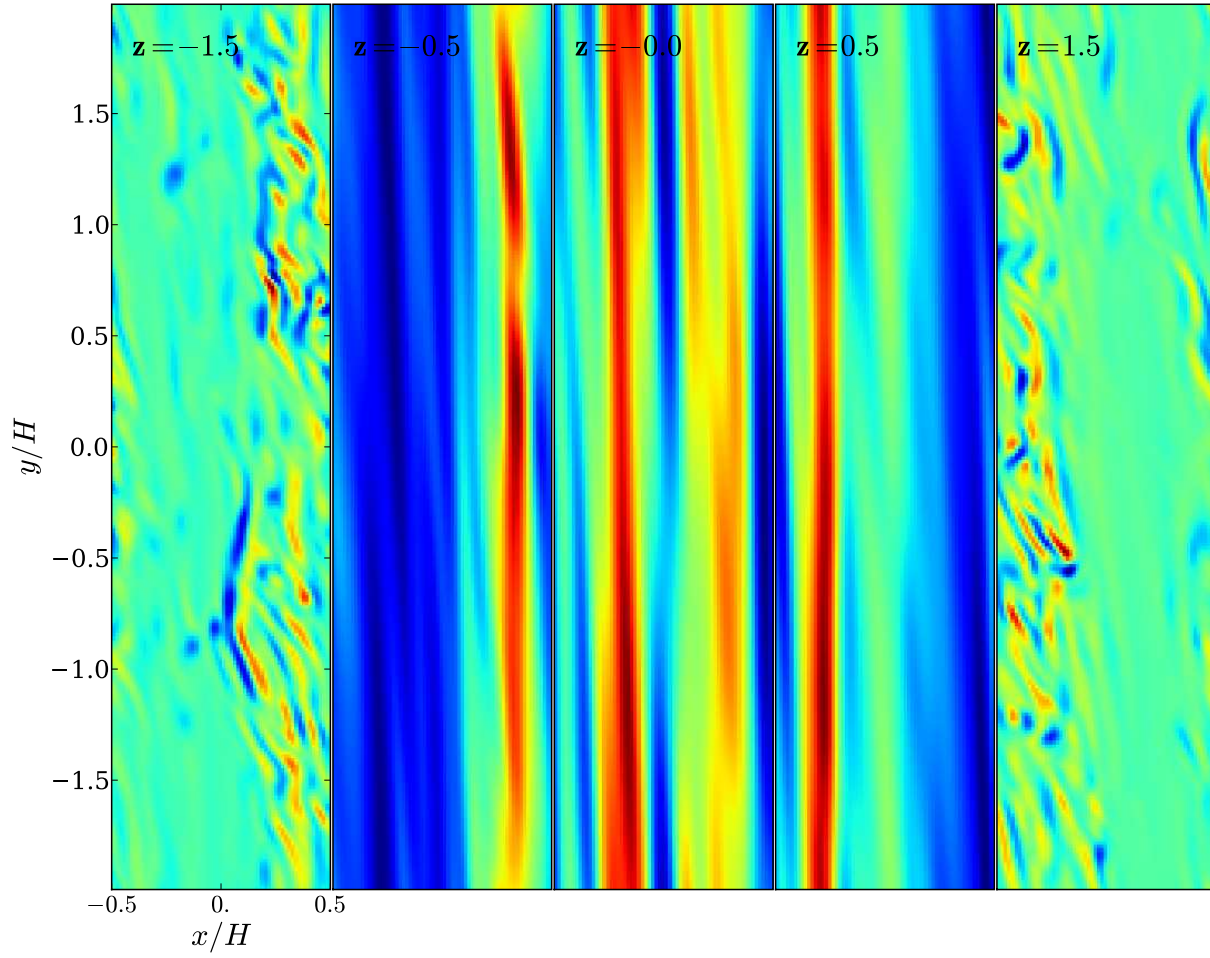


Fig. 8.— Vorticity in horizontal ( $x$ - $y$ ) planes as a function of height above and below the midplane for the  $Re_M = 3$  run. The effectively 2D nature of the flow does not appear to create regions in which coherent vortices can form.



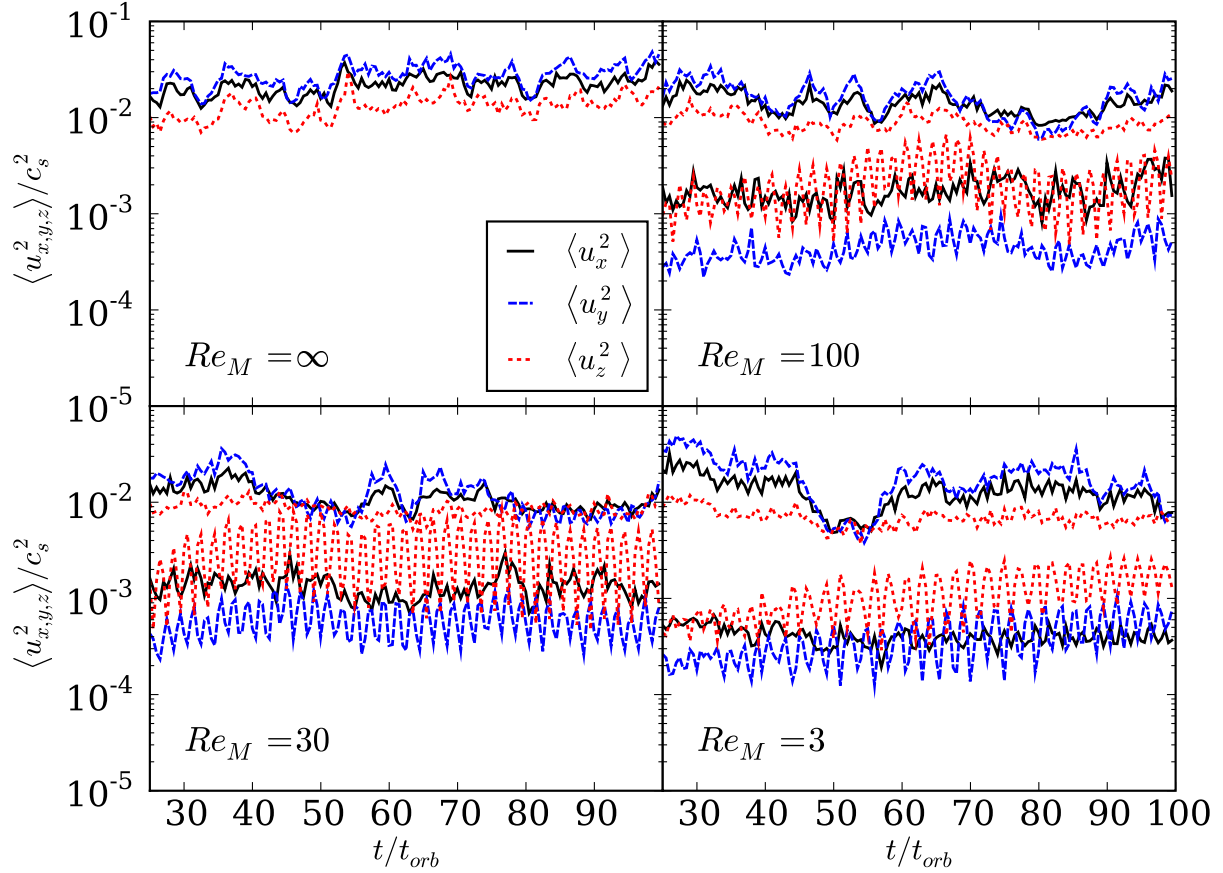


Fig. 9.— Mean square velocities in each direction for the FS runs. In all cases with a dead zone, the upper three curves show the active zone and the lower three the dead zone velocities. Note the transition in dominant component from  $y$  velocity to  $z$  velocity from active to dead in all cases.

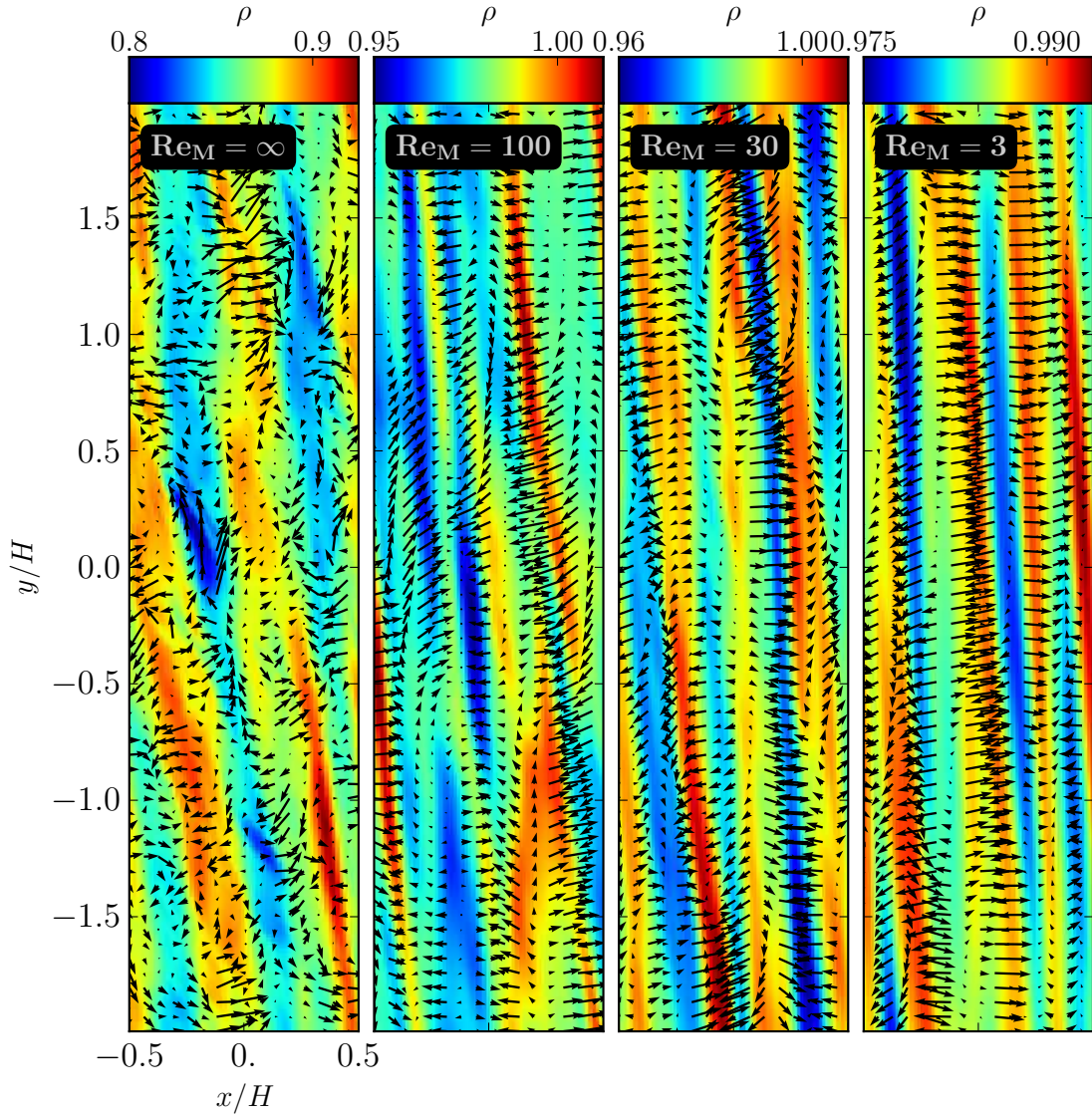


Fig. 10.— Slices through the midplane of density (color) with arrows following the in-plane ( $x$ - $y$ ) velocity. Each density image is scaled to its own minimum and maximum to emphasize morphology.

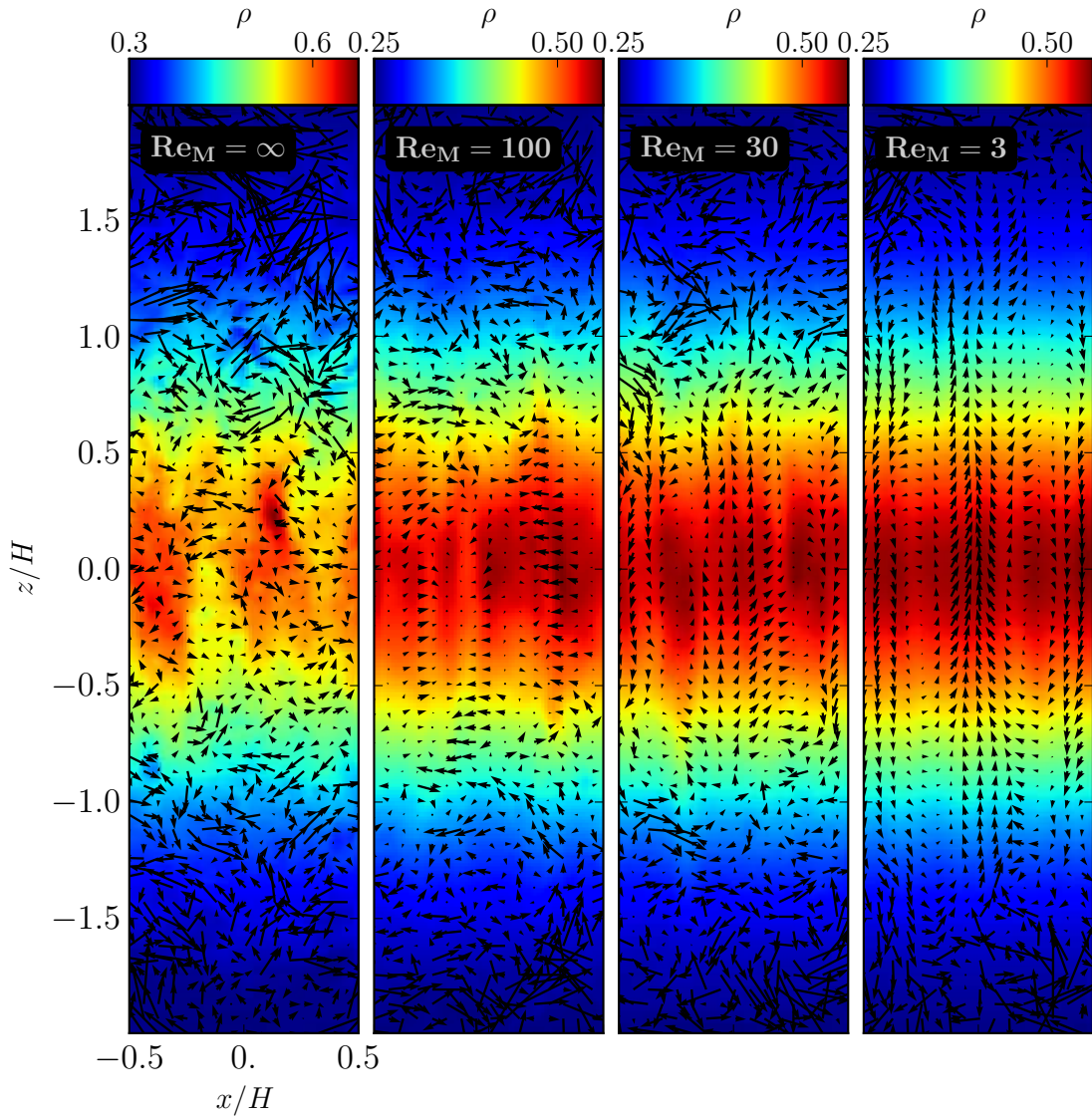


Fig. 11.— Slices through the  $y = 0$  (radial-vertical) plane of density (color) with arrows following the in-plane ( $x$ - $z$ ) velocity. Each density image is scaled to its own minimum and maximum to emphasize morphology. Note the vertical circulation in dead zones viewed in this plane.

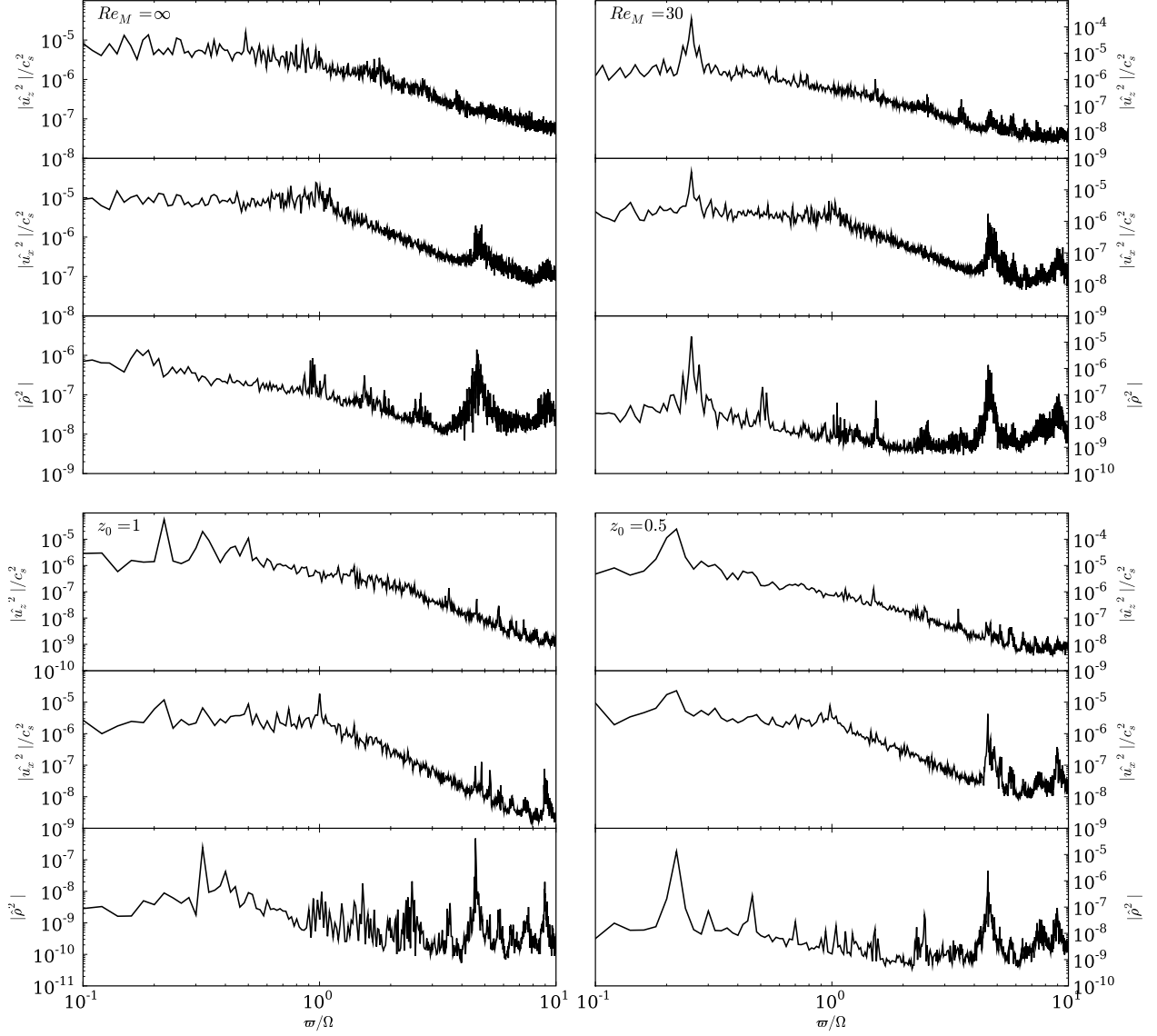


Fig. 12.— Temporal power spectra for  $u_x$ ,  $u_y$ ,  $\rho$ . Acoustic modes are present in all runs at frequencies  $> 1\Omega$ . Dead zone models also show a low-frequency inertial oscillation apparently driven by the active zones.

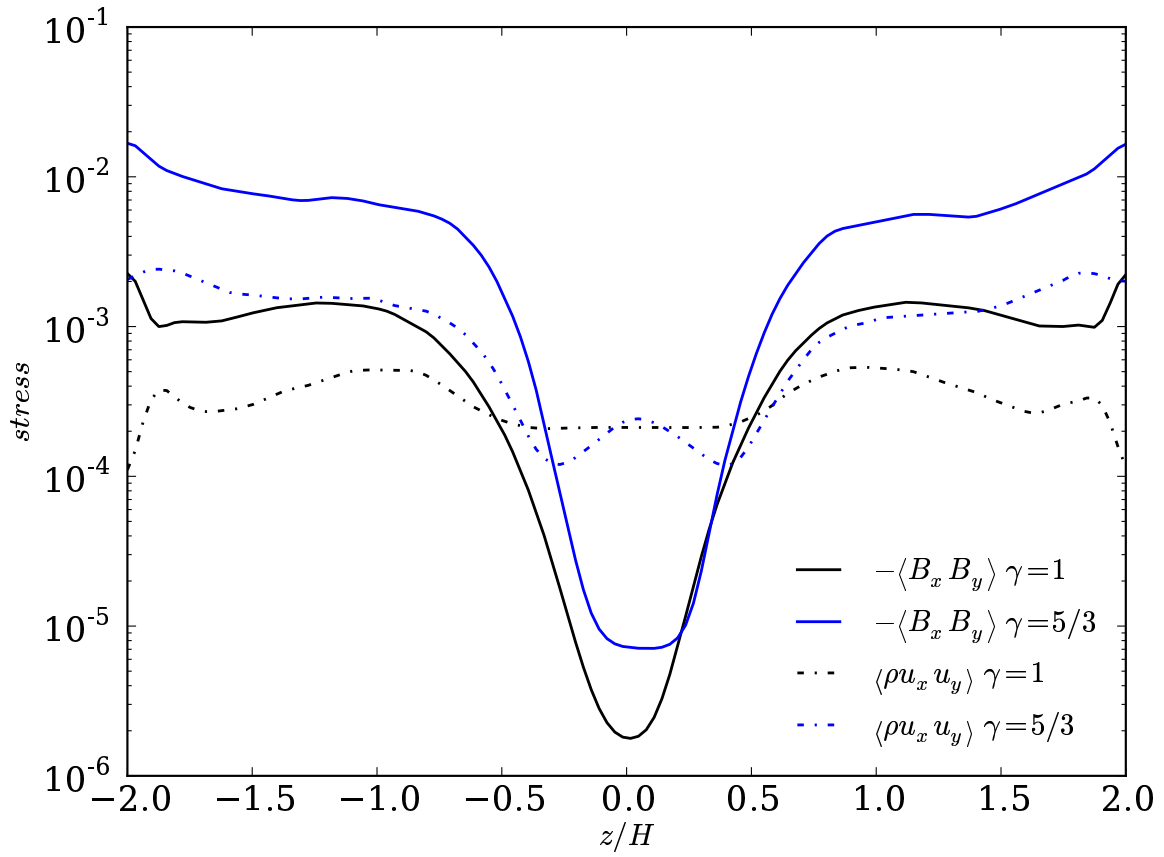


Fig. 13.— Stress vs  $z$  for isothermal and ideal gas runs.

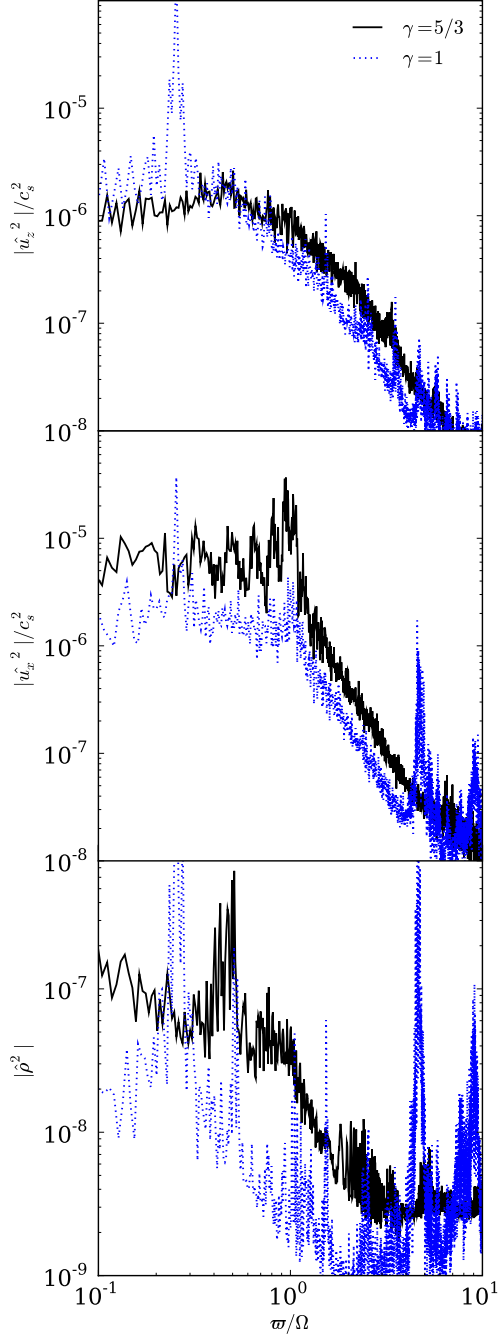


Fig. 14.— Temporal power spectra of  $u_x$ ,  $u_y$ ,  $\rho$  for  $Re_M = 30$  with ideal gas equation of state (labeled  $\gamma = 5/3$ ) and isothermal ( $\gamma = 1$ ) runs overlotted. Both inertial and acoustic waves are significantly damped but still present in the  $\gamma = 5/3$  case. The large amplitude mode at  $\varpi\Omega \simeq 0.2$  in the isothermal case remains present, though at reduced amplitude and increased wavenumber  $\varpi\Omega \simeq 0.5$ . The normalization difference between the two spectra is due to the extra heat retained in the non-isothermal case.

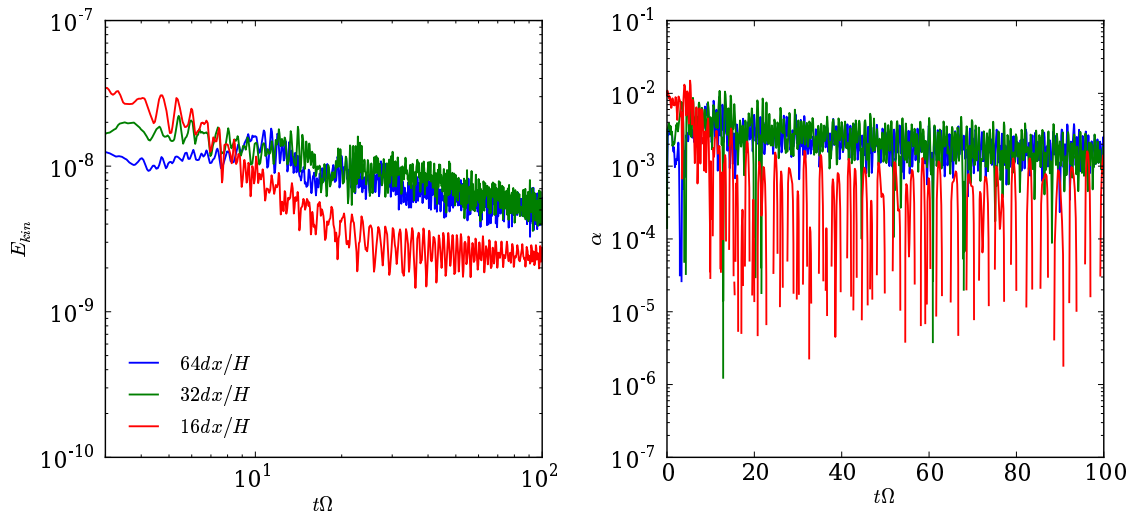


Fig. 15.— Kinetic energy and  $\alpha$  for a 2D domain with  $L_x = L_y = 4H$  at three different resolutions,  $(16, 32, 64)dx/H$ , using initial velocity perturbations of magnitude  $\sigma = 0.8c_s$ . Energy and  $\alpha$  are clearly well converged at a resolution of  $32dx/H$ .

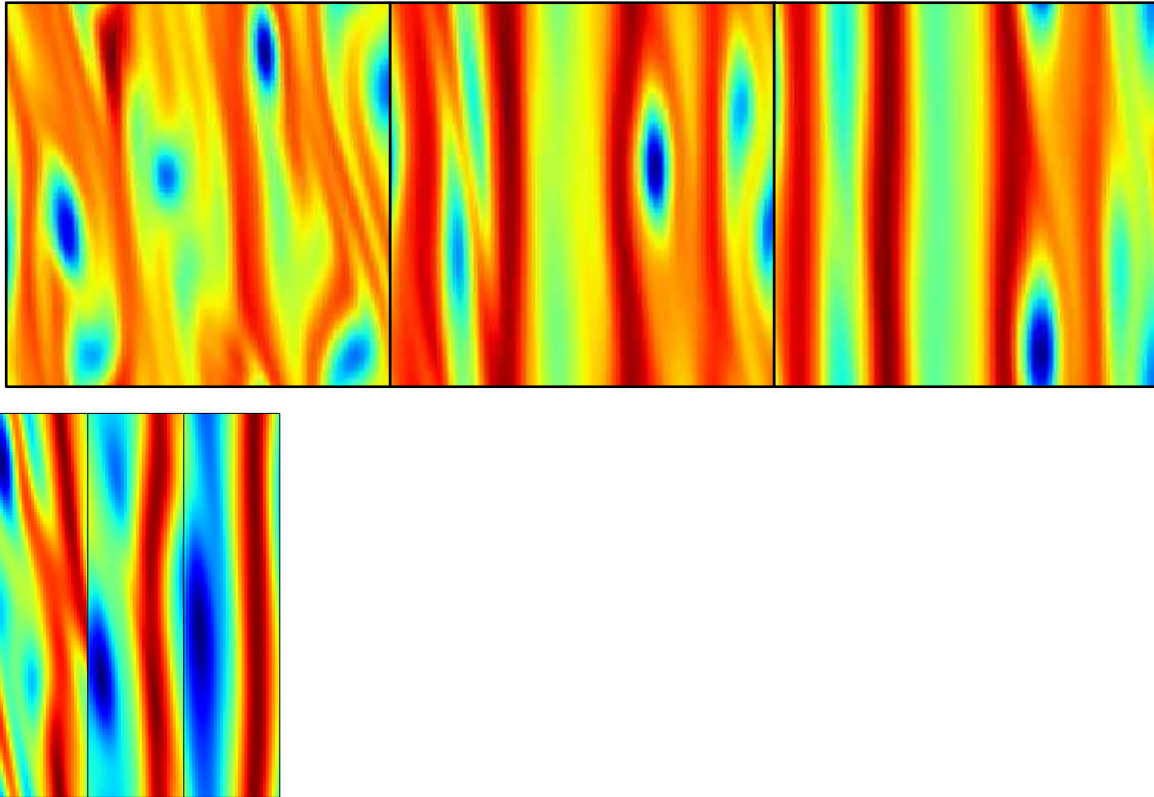


Fig. 16.— Potential vorticity of the entire  $x$ - $y$  plane at times  $t\Omega = 15.7, 31.4, 47.1$  (left to right) *upper panel* A  $4H$  square domain. Blue tones indicate negative potential vorticity, red positive. Vortex formation is similar to that found in Johnson & Gammie (2005b). *lower panel* A domain  $1H \times 4H$ . In both panels, colors are scaled to the minimum and maximum of each image to highlight vortex morphology.



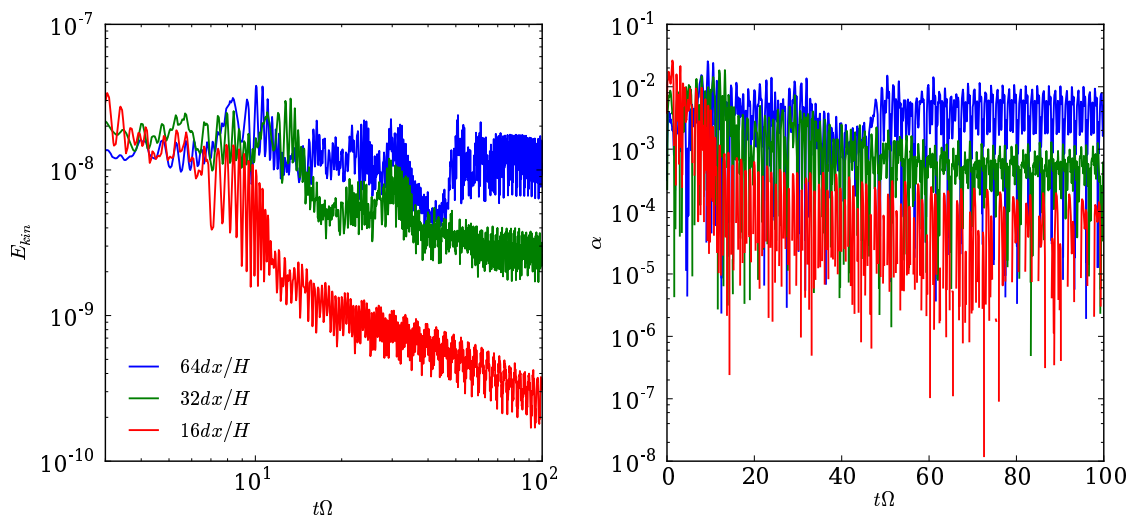


Fig. 17.— Kinetic energy and  $\alpha$  for a domain with  $L_x = 1H$ , and  $L_y = 4H$ , at three different resolutions,  $(16, 32, 64)dx/H$ , using initial velocity perturbations of magnitude  $\sigma = 0.8c_s$ . Energy and  $\alpha$  are not as well converged as in Figure 15, but sustained vortex activity does seem to occur even at 32 zones/H.

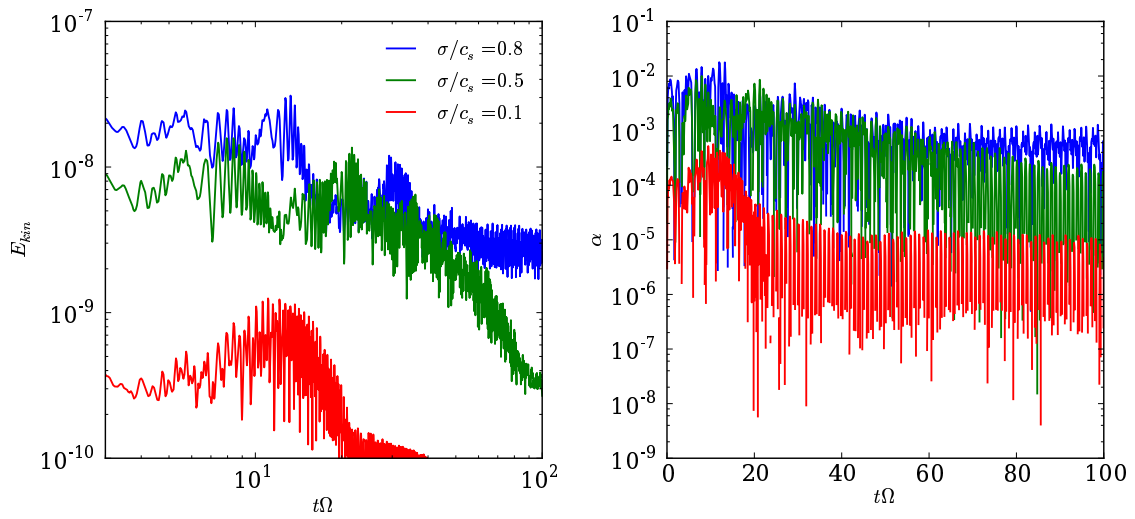


Fig. 18.— Kinetic energy and  $\alpha$  for a domain with  $L_x = 1H$  and  $L_y = 4H$  at resolution of  $32dx/H$ , using three different initial velocity dispersions,  $\sigma = (0.1, 0.5, 0.8)c_s$ . Sustained vortex activity clearly requires strong initial perturbations.

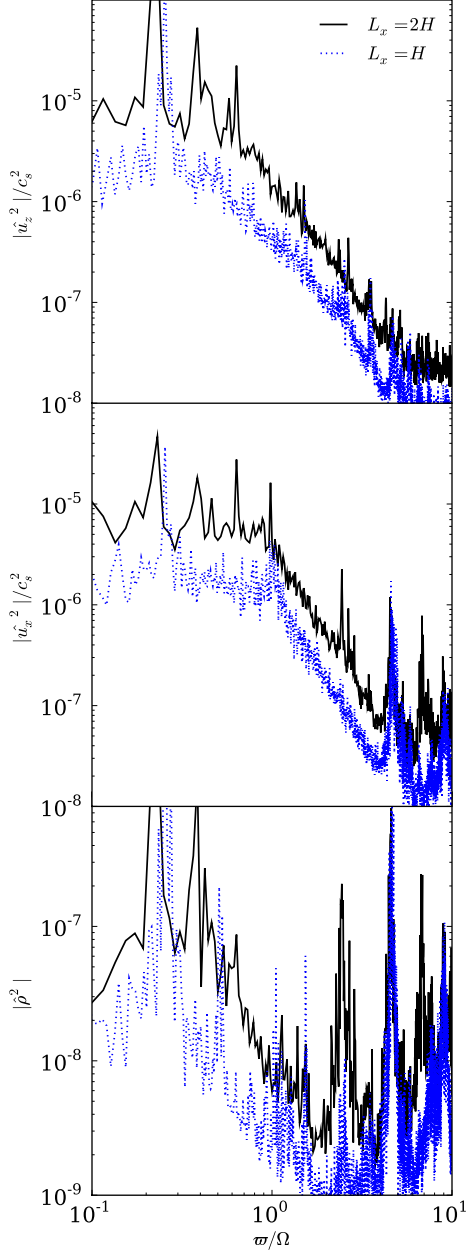


Fig. 19.— Temporal power spectra of  $u_x$ ,  $u_y$ ,  $\rho$  for  $Re_M = 30$  with the standard box width ( $-0.5H < x < 0.5H$ ) and a box twice as wide ( $-H < x < H$ ). The wider box features the large axisymmetric pressure bumps reported by Johansen et al. (2009), but this has little effect on the oscillations reported in this paper.

Table 1. Directional normalized enstrophy for dead and active zones.

Run	Active			Dead		
	$\omega_x^2/\omega^2$	$\omega_y^2/\omega^2$	$\omega_z^2/\omega^2$	$\omega_x^2/\omega^2$	$\omega_y^2/\omega^2$	$\omega_z^2/\omega^2$
64Rinf	0.31	0.34	0.35	...	...	...
64R100	0.32	0.34	0.35	0.11	0.69	0.20
64R30	0.35	0.36	0.29	0.07	0.79	0.14
64R3	0.31	0.41	0.28	0.06	0.68	0.26
32z0.5	0.26	0.48	0.27	0.10	0.68	0.22
32z1.0	0.27	0.46	0.26	0.07	0.76	0.17